Mon. Not. R. Astron. Soc. 277, 1047–1062 (1995)

The morphology and metal abundance of M86 from *ROSAT* PSPC and HRI observations: dust destruction in supersonic ram-pressure stripping

F. V. N. Rangarajan, D. A. White, H. Ebeling and A. C. Fabian
Institute of Astronomy, Madingley Road, Cambridge CB3 0HA

Accepted 1995 June 30. Received 1995 June 28; in original form 1994 December 22

ABSTRACT

From deep *ROSAT* PSPC and HRI observations of M86 (NGC 4406) we have mapped metal abundance and temperature changes across the image and detected significant structure in addition to the X-ray plume. We measure a high abundance in the plume of $Z \sim 0.65^{+0.4}_{-0.2}$ $Z_{\odot}$, which is significantly higher than the abundance in the core of M86 ($\sim 0.3 \pm 0.1$ $Z_{\odot}$) or the cluster abundance (~ 0.2 $Z_{\odot}$). The spectra from regions larger than the inner few arcmin show an enhanced silicon abundance. The galaxy and the plume are at similar temperatures $kT \sim 0.8 \pm 0.03$ keV, compared to the cluster temperature of ~ 1.9 keV. The structures detected and the abundance measurements support the hypothesis that the Virgo ICM is ram-pressure stripping the ISM of M86 in a single blob. Dust in the stripped material, previously held within cold gas clouds, is being destroyed. The morphology and calculations of the ram pressure indicate that M86 may have a southwards velocity in the plane of the sky of ~ 500 km s^{-1} compared to its radial velocity of 1374 km s^{-1} relative to the cluster.

Key words: ISM: general – galaxies: abundances – galaxies: elliptical and lenticular, cD – galaxies: individual: NGC 4406 – galaxies: ISM – X-rays: ISM.

1 INTRODUCTION

M86 (NGC 4406), a bright elliptical (SO1(3)/E3) galaxy in the Virgo Cluster, has a high negative radial velocity of 1374 km s^{-1} (Faber et al. 1989) relative to the cluster, compared to the cluster velocity dispersion of 762 km s^{-1}. It is X-ray-bright ($L_X \sim 1.7 \times 10^{42}$ erg s^{-1}, $L_B \sim 10^{11}$ $L_{\odot}$) with most of the X-rays radiated by thermal bremsstrahlung from the hot interstellar medium (ISM). Forman et al. (1979) discovered a plume of soft X-ray emission, thought to be gas stripped from M86 by ram pressure with the Virgo intracluster medium (ICM). They suggest that the galaxy may be on a radial orbit in the cluster, passing through the cluster core about every 5×10^9 yr (Forman et al. 1979; see also Fabian, Schwarz & Forman 1980; Takeda, Nulsen & Fabian 1984).

In other wavebands, a faint optical asymmetry in a direction similar to the X-ray plume (Nulsen & Carter 1987) has been noted, as well as both 60- and 100-μm infrared emission (Knapp et al. 1989; White et al. 1991), the former approximately 210 arcsec away from a source at the optical centre, the latter at the centre. Radio observations by Bregman, Roberts & Giovanelli (1988) detected 1.5×10^8 $M_{\odot}$ of H I, increased to 2.5×10^8 $M_{\odot}$ by Bregman & Roberts (1990). The H I is highly centrally concentrated in the core and appears to be not rotating, but turbulent; it is also extended along the plume. In the radio 5-GHz (6-cm) waveband M86 appears to be underluminous (Fabbiano, Gioia & Trinchieri 1989), which may be due to the ram-pressure stripping (White et al. 1991).

White et al. (1991) have analysed M86 in multiple wavebands, including optical observations and data from *IRAS* and the *Einstein* Observatory. The authors include a detailed dynamical explanation for the morphology and *IRAS* emission of M86 and for the north-west extension of the optical isophotes, in the same direction as the X-ray-emitting plume. They hypothesize that ram-pressure stripping of the ISM is exposing dust in the stripped gas to X-ray-temperature plasma which destroys it by sputtering. This is consistent with the *IRAS* 60- and 100-μm fluxes and the inferred temperatures. The optical extension is explained by starlight scattering off the exposed dust in the plume. We discuss this model in the light of the X-ray abundance and morphology results in Section 4.

M86 and the Virgo cluster have also been observed in the *ROSAT* All Sky Survey (Böhringer et al. 1994), by *Ginga* (Takano et al. 1989), and by *EXOSAT* (Edge 1990). It has recently been observed by *ASCA*, and preliminary abundance and temperature results were obtained (Awaki et al.

1994; Matsushita et al. 1994). We discuss these in detail in Section 3.3. The surrounding cluster emission has been studied during a pointing at M87 (Stewart et al. 1984).

This paper reports a detailed X-ray analysis of Position Sensitive Proportional Counter (PSPC) and High Resolution Imager (HRI) data, which together use the full capabilities of *ROSAT*: a spectral resolution of about five bands from 0.2 to 2 keV and a spatial resolution of 1.7 arcsec (FWHM). We assume a distance to Virgo of 20 Mpc, i.e. a size scale of 6 kpc arcmin^{-1}. The Galactic H I column density along the line of sight to M86 is taken to be 2.6×10^{20} cm^{-2} (Stark et al. 1992). We first present adaptively smoothed images of M86 with the HRI and PSPC. We next investigate structure in the HRI image, and map the morphology of M86, then present a set of spectral models for eight interesting regions.

2 THE HRI IMAGE

M86 was observed with the *ROSAT* HRI on 1992 June 27, 1992 December 13 and 1994 June 13 for a total of 12 578 s. The pointing at RA = $12^h26^m12^s$, Dec. = 12°57′00″ (J2000) shows M86 well centred within the detector and includes the whole of the plume.

To identify potential structure in the image, two adaptive smoothing algorithms were used on the data: one within the FTOOLS set of data manipulation software, and one developed by us to check that, and for further statistical tests. Both employ a variable radius top-hat smoothing which depends on the surface brightness of the region being smoothed. A significance level is chosen which implies a particular number of counts to smooth over (the algorithm maintains at least that number of counts within the smoothing region). Both algorithms produce the same results in all images smoothed. The images presented here were generated using the FTOOLS adaptive smoothing algorithm FADAPT.

These algorithms tend to redistribute counts on many scales. Substructure that is both statistically and visually apparent appears on the *count* scale set in the smoothing. Circularly symmetric blobs containing the set number of counts appear around the brightest pixels in a region. These blobs contain enough counts to be statistically significant features. However, their *comparative* significance is low if several similar blobs appear in a region. Each blob is a statistically quasi-independent pixel created by the adaptive smoothing, and substructure on the blob scale is therefore potentially spurious. This effect diminishes when we set a high significance, and thus count level for the algorithm. We therefore test the significance of substructure identified in the adaptively smoothed images *in the raw photon data*. The adaptively smoothed images we present here (Figs 1 and 2) use a smoothing count-level which allows the structure we identify as significant from the raw data to remain, but does not generate artificial substructure.

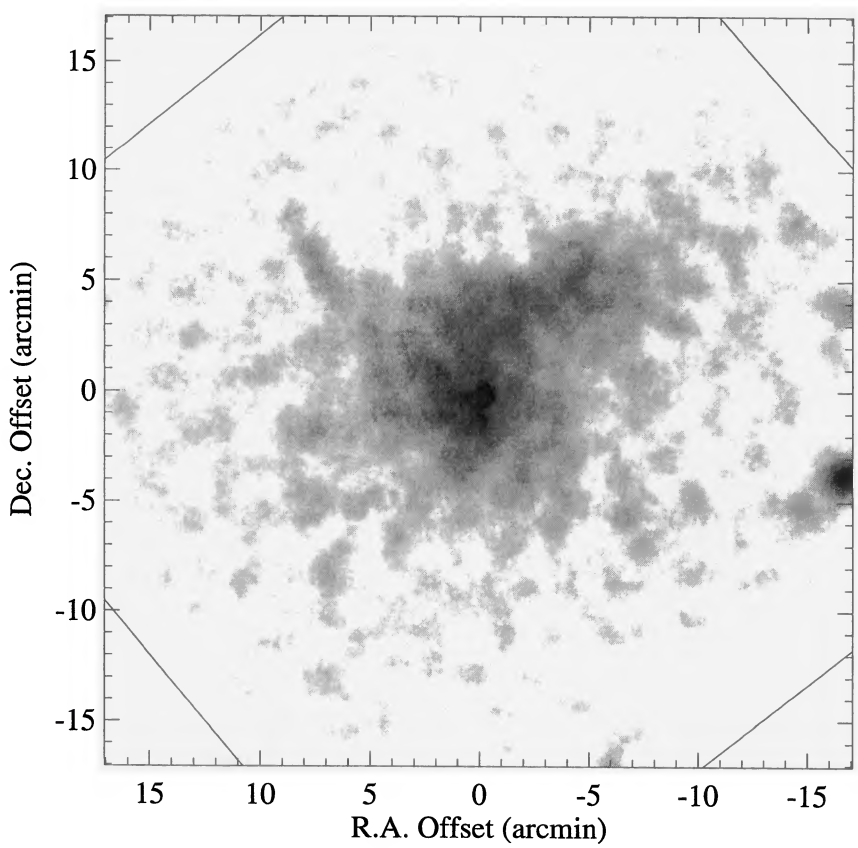

Figure 1. An adaptively smoothed image of M86 with the HRI, binned into 2-arcsec pixels. The smoothing was performed using a minimum of 100 counts per circular smoothing bin. The brightness scale is logarithmic, from 36 to 900 count arcmin^{-2}. The pointing was RA $12^h26^m12^s$, Dec. 12°57′00″. The lines at the corners mark the edge of the original HRI image. M84 can be seen on the western edge of the image, with a loop of emission to the south-east.

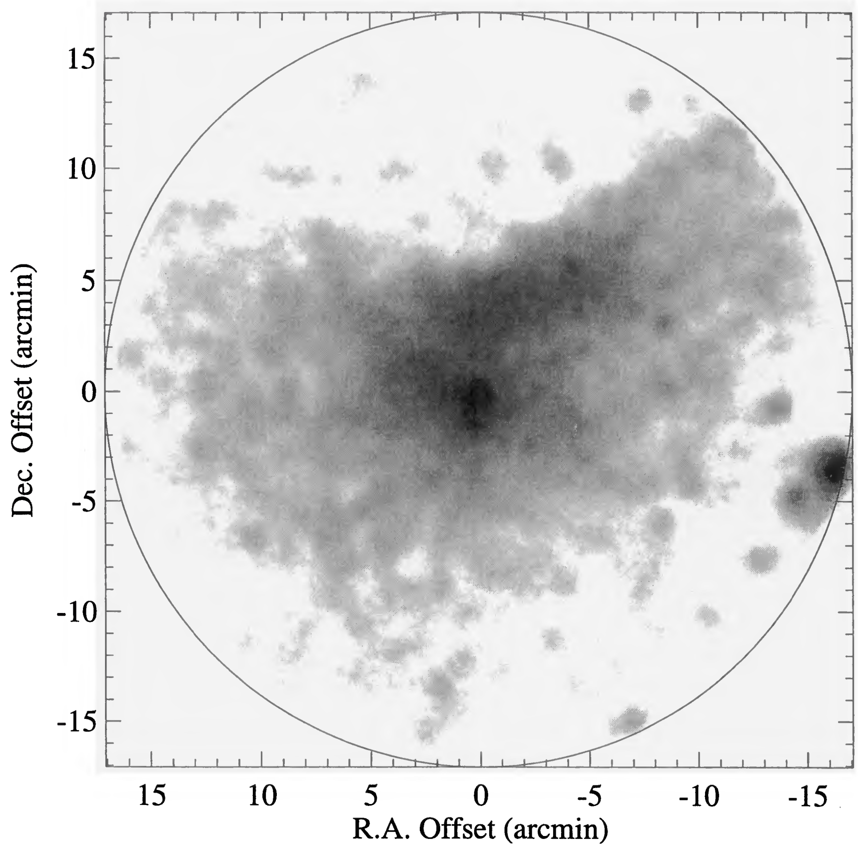

Figure 2. An adaptively smoothed image of M86 with the PSPC, binned into 4-arcsec pixels. The smoothing was performed using a minimum of 100 counts per circular smoothing bin. The brightness scale is logarithmic, from 45 to 2700 count arcmin^{-2}. Note the extreme sharpness of the northern edge, clearer here than in the HRI image due to the low background of the PSPC. The pointing was RA $12^h26^m12^s$, Dec. 12°57′00″. The enclosing circle marks the edge of the area chosen for the adaptive smoothing. M84 can be seen on the western edge of the image, with a loop of emission to the south-east.

We use a pixel size of 2 arcsec for the HRI image. However, the adaptive smoothing can be considered as rebinning with a bin size that varies across the image. The small pixel size allows the algorithm the greatest dynamical flexibility to detect structure in regions of high surface brightness, but is essentially ignored at low surface brightness levels where the algorithm selects the statistically appropriate, much larger, bin size. The smoothing scale at the lowest level is of the order of 0°.1; however, in the core of M86 the smoothing scale is of order arcseconds.

Using the adaptively smoothed images (Figs 1–3), we identify four statistically significant structures, shown marked on a contour plot of the HRI image smoothed with a fixed Gaussian (Fig. 4). To test the apparent substructure, we select an appropriate radial, azimuthal or linear rebinning of the raw photon data, which must show the same structure with at least a 3σ signifcance. These plots are shown in Figs 5–9.

(i) *The X-ray plume* is clearly detectable at radii as great as 0°.2 (~70 kpc). Figs 7 and 9 show the plume clearly from 1 to 12 arcmin from the core. It shows a significant brightening near 0°.14 to the north-west, seen best in the PSPC slice shown in Fig. 11 because of the higher sensitivity and lower background of the PSPC, and the longer observing time. Fig. 11 shows a surface brightness profile along the length of the plume. We do not discuss the end brightening further, as it is not unambiguously detected in the HRI image.

(ii) *A southern extension* which starts from 0.5 arcmin from the core and extends to about 3 arcmin (Figs 8 and 7). The core itself within 1 arcmin appears to show such an asymmetry when smoothed, but the statistics within 30 arcsec do not permit further investigation (the raw counts in 2-arcsec bins in the core vary from 0 to 4). The extension is clearly visible in Fig. 3.

(iii) *A hole* at RA offset 1.79 arcmin, Dec. offset 1.94 arcmin. The hole is close to circularly symmetric and is not clearly connected to the low surface brightness at larger radii from M86, shown by the lack of azimuthal variation in a circle centred on the hole (Fig. 6). It is highly significant (Fig. 5). The hole can also be seen in Fig. 11, between the main plume and the north-eastern arm. We have constructed detector coordinate maps of the counts surrounding the hole to check if a detector defect or a chance superposition of the support wires may cause the hole, but the 14 closest counts are spread over 5×5 arcmin^2. The hole appears to be real and does not seem to be connected to the low surface brightness region further east.

(iv) *The north-eastern arm* starts at the core and extends to at least 5 arcmin (Fig. 7). After a couple of breaks (Fig. 1), it appears to extend out to 12 arcmin (Fig. 9). Whether these two structures are in fact related is indeterminable from

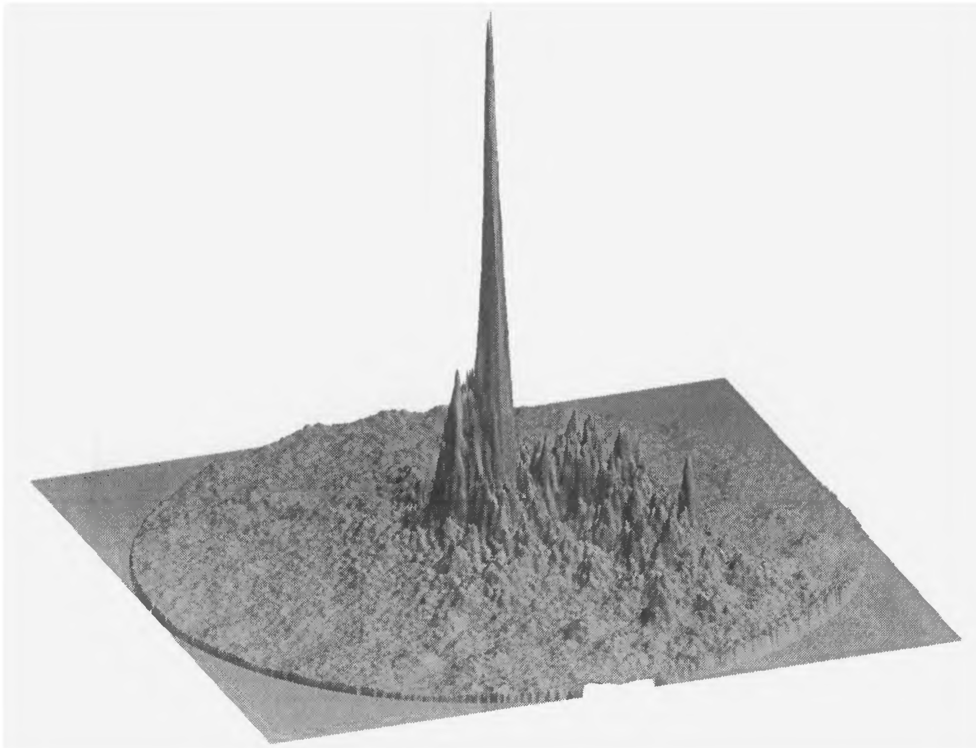

Figure 3. A 3D plot of the surface brightness of the adaptively smoothed PSPC image of M86, binned into 4-arcsec pixels. The smoothing was performed using a minimum of 100 counts per circular smoothing bin. The brightness Z-axis is linear, from 45 to 2700 count arcmin^{-2}. South is towards the bottom left. Note the plume extending to the north-west and the southern core extension. The lower surface brightness to the north can just be seen. The radius of the image of 12.8 arcmin.

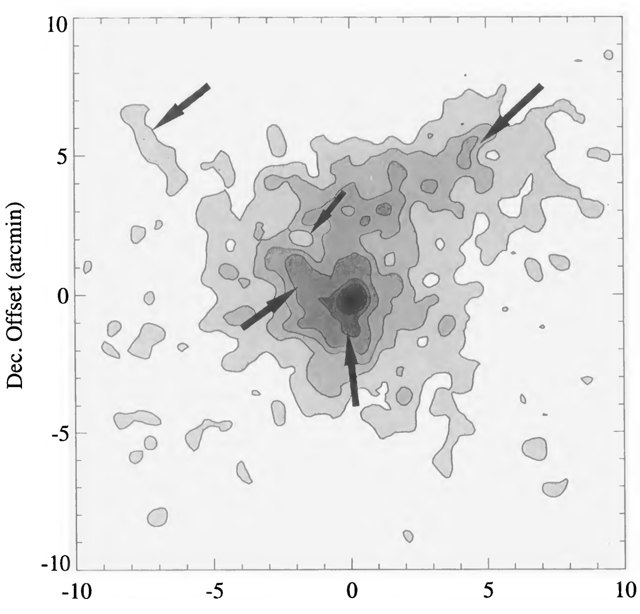

Fig. 4. A contour plot of M86 with the HRI, binned into 8-arcsec pixels and smoothed at a fixed size-scale of 2 bins. Note that even this heavy smoothing reveals much the same structure as the adaptive smoothing. The marked areas are discussed in the text; from left to right: the north-eastern arm at large radii, the arm near the core, the hole, the southern extension, and the plume with its bright end.

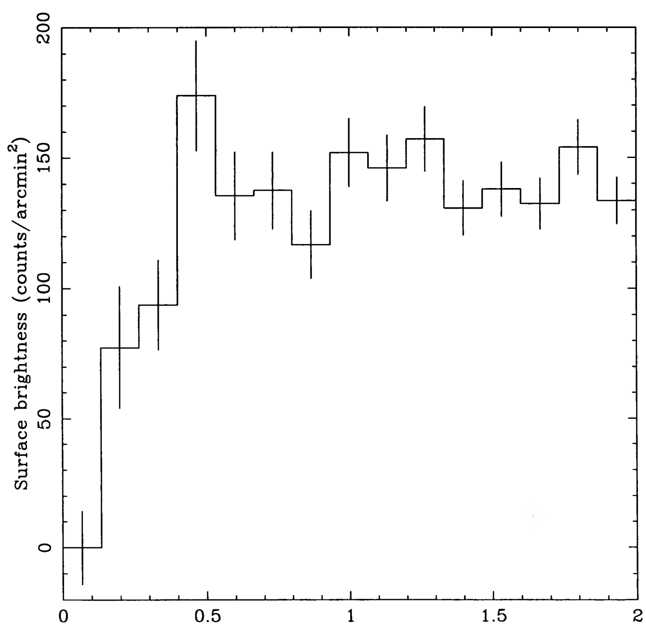

Figure 5. A *radial* plot of counts in a circle radius 2 arcmin centred on the *hole* in the unsmoothed 8-arcsec binned HRI image of M86 at RA offset 1.79 arcmin, Dec. offset 1.94 arcmin. The lack of counts in the hole is significant at over 10σ. It is reasonably circular, as can be seen by comparing this plot to an azimuthal plot of surface brightness around the same point to the same radius (Fig. 6).

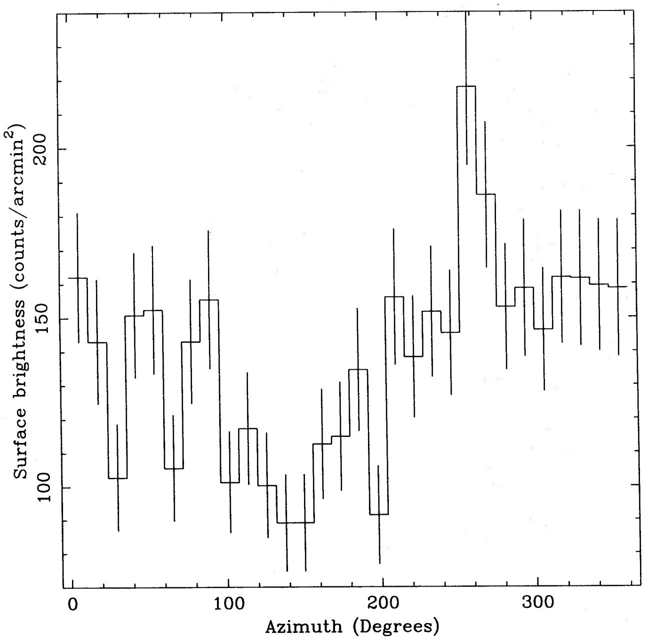

Figure 6. An *azimuthal* plot of counts within a circle radius 2 arcmin centred on the *hole* in the unsmoothed binned HRI image of M86 at RA offset 1.79 arcmin, Dec. offset 1.94 arcmin. Due west is defined as 0°, north is 90°. The level remains relatively constant and high compared to the surface brightness in the hole (see Fig. 5). The brightening at around 270° is due to the north-eastern arm, just south of the hole; the dimming at around 120° is towards the north-east, away from the core and roughly parallel to the north-eastern arm.

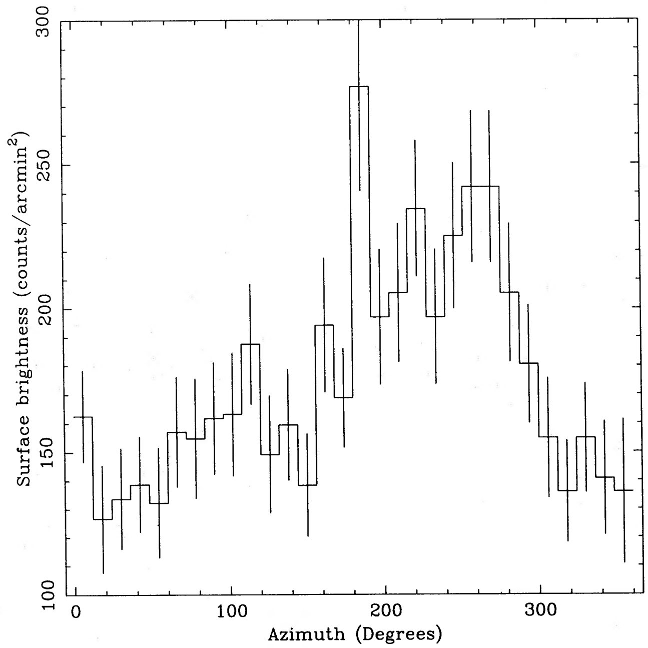

Figure 8. An *azimuthal* plot of counts within an annulus from 0.5 to 2 arcmin in the unsmoothed binned HRI image of M86, centred on the brightest pixel at RA offset −0.16 arcmin, Dec. offset −0.13 arcmin, the *core* of the galaxy. Due west is defined as 0°, north is 90°. This shows the asymmetry in emission close to the core, with a substantial brightening towards the south, at around 270°.

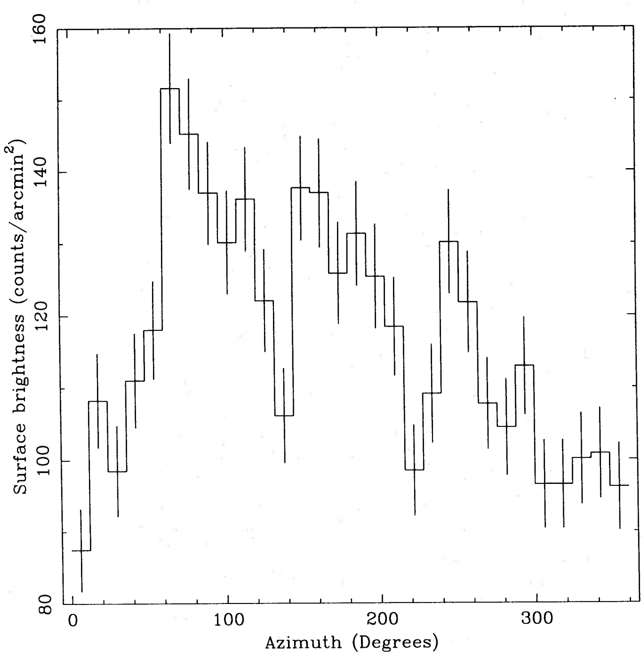

Figure 7. An *azimuthal* plot of counts within an annulus from 1 to 5 arcmin centred on the brightest pixel of the unsmoothed binned HRI image of M86 at RA offset −0.16 arcmin, Dec. offset −0.13 arcmin, the *core* of the galaxy. Due west is defined as 0°, north is 90°. This plot clearly shows the three source extensions from the centre – the plume at 90°, the north-eastern arm at 140°–180°, and the core asymmetry to the south at 250°.

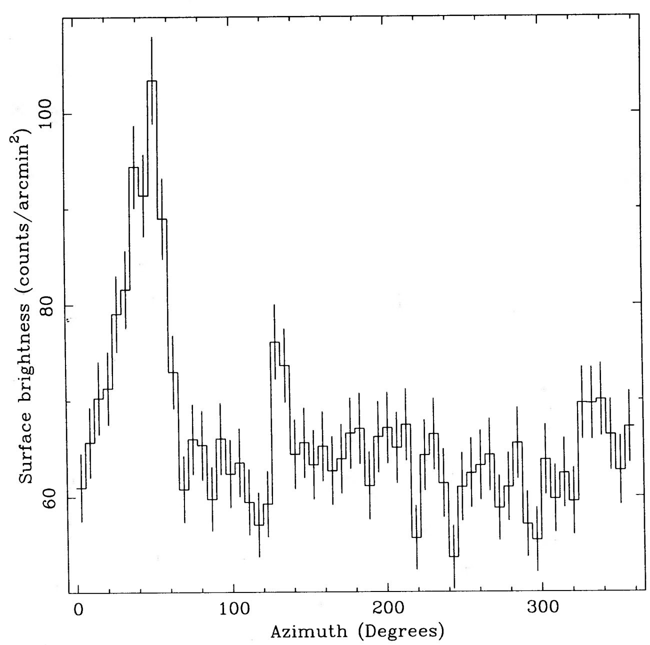

Figure 9. An *azimuthal* plot of counts within an annulus from 7 to 12 arcmin in the unsmoothed binned HRI image of M86, centred at RA $12^h26^m17^s$, Dec. 12°58′24″ (J2000), RA offset 1.21 arcmin, Dec. offset −1.41′, 1′51″ to the south-east of the core, in line with the *arm*. Due west is defined as 0°, north is 90°. This shows two particular features: the end of the plume from 20° to 60°, and the faint, but significant, north-east arm at 130°, extending out to 12 arcmin.

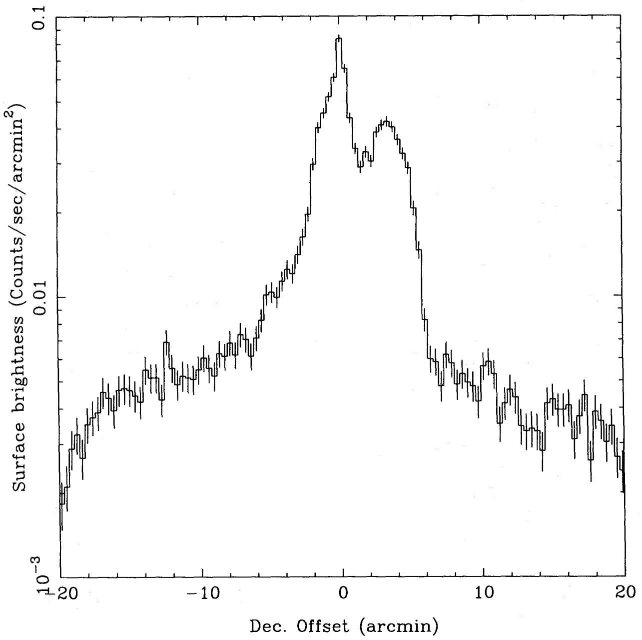

Figure 10. A north–south cut through the unsmoothed PSPC image of width 3 arcmin. This profile extends on either side to the inner support ring of the PSPC, which casts its shadow at ± 20 arcmin. It shows the asymmetry of the core, with an extension to the south, the strength of the core in the plume, and the very steep decrease in surface brightness further north.

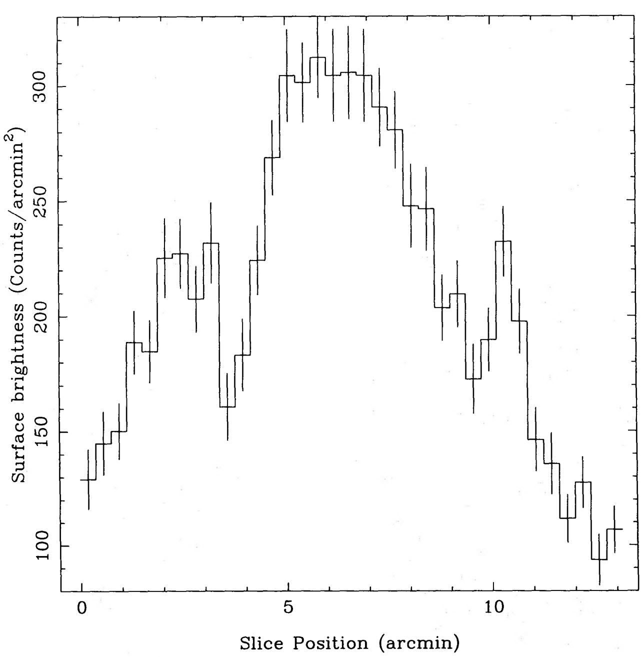

Figure 11. A linear slice through the PSPC image of the X-ray plume of M86. The slice is centred on RA $12^{\mathrm{h}}26^{\mathrm{m}}09\overset{\mathrm{s}}{.}18$ Dec. $13°00'19''$, RA offset -0.69 arcmin, Dec. offset $+3.32$ arcmin at an angle of 30° to the west, has a length of 13 arcmin and a width of 1.8 arcmin. This is essentially the length of the plume. Increasing slice position is toward the north-west. Four structures are visible: the north-eastern arm at 2–3 arcmin, the hole at 3.5 arcmin, the plume itself from 5 to 13 arcmin with the end brightening at 10.5 arcmin.

these data. Fig. 11 also shows the arm, at 2–3 arcmin. The arm appears to be of order 1 arcmin wide at radii greater than 5 arcmin from the core.

M84 is clearly detected in both observations, and both show a curious extension of emission to the south-east, which appears to be a loop when adaptively smoothed. The surface brightness is too low for further investigation.

The plume shows substructure on many size scales, but this appears to be dependent on the smoothing scale used. However, although the number of blobs and their size in such substructure vary with different significance thresholds in the adaptive smoothing algorithm, about five such blobs appear in all images with scales from 5 to 100 counts per smoothing region. Some of these can be seen in Fig. 2. The significance of these blobs was tested in one and two dimensions: linear profiles through the original data in the core of the plume were fitted with linear models, and images of the region with flat models. On several size scales and different pixel sizes the calculated χ^2 indicates that the distribution of counts is *consistent* with a flat, zero-parameter model (the mean is fixed) at the 90 per cent level; we use the appropriate χ^2/ν value for the number of pixels tested.

Following White et al. (1994), we set limits on the pixel-to-pixel count-rate variation. We construct a smooth model of the plume by smoothing the original data (4-arcsec pixel size) with a Gaussian filter 4 pixels wide. The pixel count rates in this smoothed model are $S(x, y)$, and the original data are called $I(x, y)$. The variation in observed count rate, $\delta I/I$, is assumed to have two components, one from Poisson noise (σ_{P}^2), the other real variation in the source (σ_{S}^2), i.e.

$$\sigma^2 = \sigma_{\mathrm{P}}^2 + \sigma_{\mathrm{S}}^2 \tag{1}$$

and $\sigma_{\mathrm{P}}^2 = S(x, y)$ from Poisson statistics. The equation for χ^2 then becomes

$$\chi^2 \equiv \sum_{i=1}^{N_x \times N_y} \frac{[I(x, y) - S(x, y)]^2}{S(x, y) + \sigma_{\mathrm{S}}^2}, \tag{2}$$

where N_x and N_y are the number of pixels on each side of the selected region. As $\delta I/I = \sigma_{\mathrm{S}}/S(x, y)$,

$$\chi^2 = \sum_{i=1}^{N_x \times N_y} \frac{[I(x, y) - S(x, y)]^2}{S(x, y) + S(x, y)^2 (\delta I/I)^2}. \tag{3}$$

The distribution of χ^2 itself is $P(\chi^2/\nu)$ where $\nu = (N-1)$, and N is the number of pixels $N = N_x \times N_y$. At large ν (>30), we can make the approximation

$$P(\chi^2/\nu) \approx P\left(\frac{\chi^2 - \nu}{\sqrt{2\nu}}\right), \tag{4}$$

equation (26.4.11) from Abramowitz & Stegun (1965). The 90 per cent minimum limit of the single-tail χ^2 distribution is when $\chi^2/\nu \sim 1.65$; therefore

$$\chi^2_{90\,\mathrm{per\,cent}} = \nu - 1.65\sqrt{2\nu}. \tag{5}$$

This 90 per cent lower limit on χ^2 corresponds to the 90 per cent upper limit on $\delta I/I$. Comparing the raw data to the smoothed model in a region at the centre of the plume using 21×21 pixel on a pixel scale of 4 arcsec, we find $\delta I/I < 0.18$. In some regions, those where small-scale structure appears in images adaptively smoothed on several significance levels, the variation is up to $\delta I/I < 0.54$ (10×10 pixel). In a region covering most of the plume (51×51 pixel, 3.4×3.4 arcmin^2) we find $\delta I/I < 0.14$. To test the effect of the fixed-scale smoothing level used to construct the $S(x, y)$ model, these limits were re-evaluated using $S(x, y)$ constructed with the same pixel size but smoothed on a 2-pixel scale, a level at which substructure still remains in the plume region. The same regions show $\delta I/I < 0.11$ for the plume centre and $\delta I/I < 0.48$ for the highest peaks. However, the whole plume is consistent with $\delta I/I \sim 0$, as the smoothing is light enough to leave most of the substructure. This is *not* the significance of the plume itself – it is the significance of small-scale substructure on the pixel scale in the plume after comparison with a fixed-scale smoothed model. However, the high peaks still show variations of a factor of 2. Changing the pixel size to 16 arcsec lowers these limits to be consistent with zero – there appears to be no significant variation on this pixel scale in the PSPC image. All background regions in the PSPC image are consistent with $\delta I/I \sim 0$ for areas larger than 3×3 arcmin^2. Smaller areas can be selected to produce a higher $\delta I/I$, but this vanishes when the area is expanded.

Using the HRI image with a 2-arcsec pixel size gives $\delta I/I \lesssim 0.4$ in the plume. Using a pixel size of 4 arcsec $\delta I/I < 0.2$. These limits are calculated using a comparison model generated from the smoothed data. When compared to a flat model with the same mean surface brightness $1 < \delta I/I < 2$, $\chi^2/\nu \sim 1$, showing that the plume does not exhibit statistically significant difference from a flat distribution, but that the number of counts in these images is not sufficient to constrain this substructure adequately. Note that it is necessary to avoid the Poisson small number limit in $S(x, y)$ when calculating $\delta I/I$ in regions of low surface brightness. When binned to a pixel size with greater than 7 count pixel^{-1}, or using areas larger than 5×5 arcmin^2, the background regions of the HRI image are always consistent with $\delta I/I \sim 0$.

This $\delta I/I$ statistic is sensitive only to repeated variations in surface brightness on the pixel scale. Because it is totally insensitive to pixel correlations and extended substructure, the pixel scale is important. Individual blobs of emission may be real and yet contribute little to the statistic; however, visual inspection and the adaptive smoothing suggest that there is substructure in the plume. Thus the adaptive smoothing of the HRI and PSPC images and these limits on $\delta I/I$ are suggestive of substructure but are not sufficient to confirm this substructure at a significant level. We await with great interest missions with higher resolution and effective area observing this region.

In summary, we detect significant structure in the X-ray image, all of which is present in both the PSPC and HRI images. The plume shows a complex morphology, and may have substructure. A north-eastern extension extends to 5 arcmin, and is in line with an arm out to 12 arcmin only 1 arcmin wide. The plume and the north-eastern extension are separated by a significant hole, which appears to be roughly symmetric and where no counts at all are seen. The core shows a surface brightness extension towards the south.

3 THE PSPC OBSERVATION

M86 was observed with the *ROSAT* PSPC on 1991 December 16, for a total of 22 296 s. The pointing was RA = $12^{\mathrm{h}}26^{\mathrm{m}}12^{\mathrm{s}}$, Dec. 12°57′00″ (J2000) which is 1°22′ to the north-west of the centre of M87. An adaptively smoothed image (Fig. 2) shows the same structures as were detected in the HRI image. The northern edge is sharper in the PSPC image (Fig. 2) than the HRI image (Fig. 1) because the HRI has a higher internal background.

Fig. 10, a north–south slice through the PSPC image, shows the great symmetry in M86. It emphasizes the brightness of the plume core, at +4 arcmin from the centre, and the extremely sharp decrease in surface brightness just north of this at +5 arcmin. The PSPC shows significant structure in the plume core, which we map in greater detail with the HRI (see Section 2).

Fig. 12 shows the strong asymmetric emission from M87 and the cluster medium which results in a gradient of cluster emission across M86 in both RA and Dec. (Fig. 13). The gradient appears to be smooth and spectrally consistent with cluster emission; a similar profile in 0.2–0.5 keV emission does not appear to be affected by the North Polar Spur (NPS). However, the cluster gas and emission local to our Galaxy imply that there must be multiple soft background spectral components in the field of view. We map the cluster emission and fit an interpolated background spectrum to minimize its effect and account for the local soft background and the hard extragalactic X-ray background (see Section 3.1).

Hardness and softness ratio maps show no apparent background point sources after source subtraction, nor areas of spectral variation uncorrelated with the cluster and galactic emission. The emission in the core of M86 is much softer than the cluster gas. Contours in both hardness and softness maps enclose the same regions as those of the surface brightness (Fig. 14). The maps also show the temperature gradient in the cluster emission.

We considered the possibility that emission from the NPS, a Galactic superbubble feature, extends into the field of view. The NPS is very diffuse and extends over 90° of the sky. It contaminates the cluster in the south-east corner. A soft image of the cluster (Böhringer et al. 1994) indicates that it has little effect at the location of M87 and M86. To the south-east of M87 it is only by means of the spectrum that cluster emission and the NPS can be distinguished, as the NPS has a temperature of a few million degrees (Böhringer 1994, private communication). We therefore do not include extra emisison from the NPS in the spectral models, but caution that such extra soft emission may imply that the column densities found in Virgo by X-ray spectral fitting are underestimated, and that the column densities obtained by the *ROSAT* PSPC depend solely on data below 0.5 keV, where there are large systematic uncertainties. Given these complications, we placed great importance on obtaining a realistic and physically plausible background model.

3.1 Background subtraction

Spectra from four regions away from M86 were analysed to constrain the surrounding cluster emission and background components. (Note that we will use the term 'background' to refer to the combined contaminating cluster and non-cluster emission, unless stated specifically.) An annulus from 0°.35 to 0°.8, centred on M86 and outside the PSPC support ring, was source-subtracted and the support spokes masked out. This

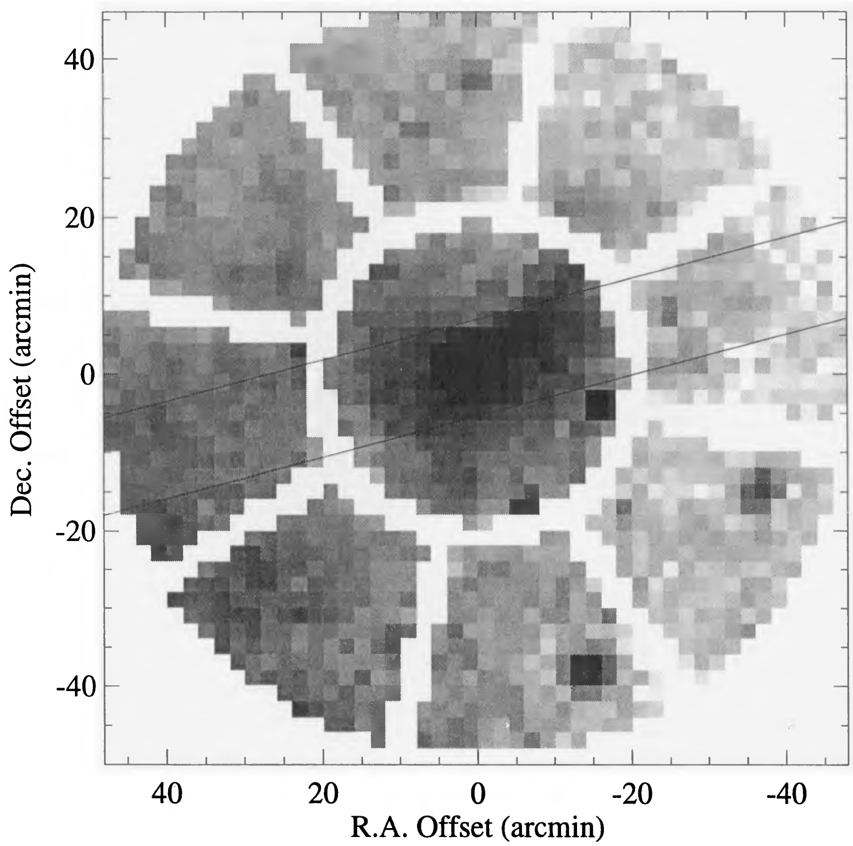

Figure 12. The PSPC image of M86, binned into 2×2 arcmin^2 pixels and vignetting-corrected, showing the emission to the south-west which is from gas connected with M87. The emission has a strong gradient in both RA and Dec. The PSPC support ribs have been masked out. The parallel lines enclose the area for which a surface brightness profile appears in Fig. 13.

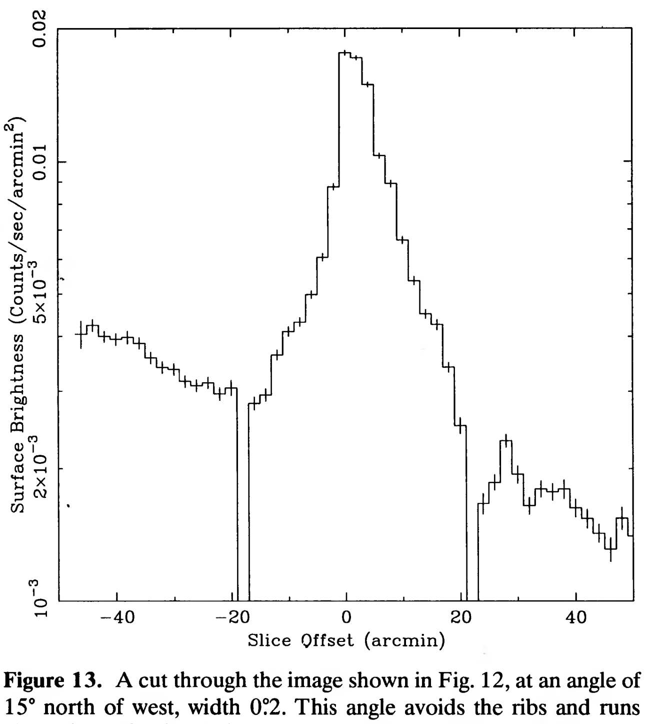

Figure 13. A cut through the image shown in Fig. 12, at an angle of 15° north of west, width 0°.2. This angle avoids the ribs and runs along the main ridge of background emission. It shows the strong gradient in emission from gas connected to M87. The shadow of the PSPC support ribs can be seen at ±20 arcmin. The profile is vignetting-corrected.

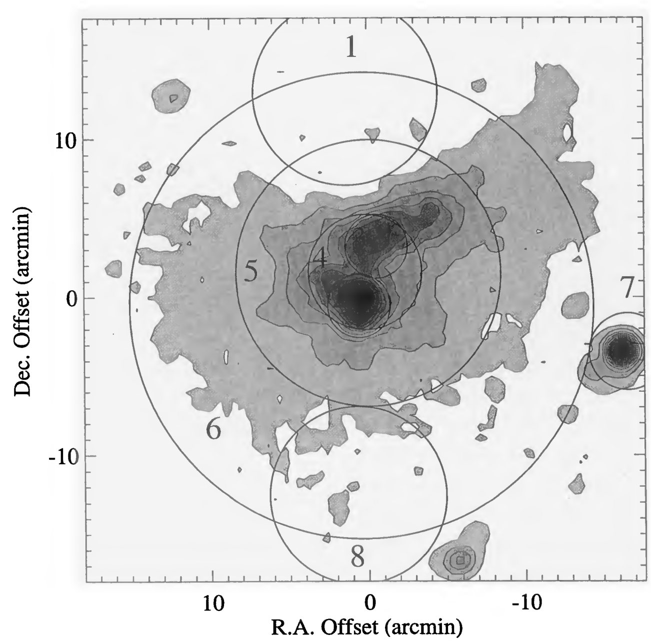

Figure 14. The areas investigated spectrally, superimposed on a contour map of top-hat fixed-scale smoothed PSPC data. The positions and sizes of the numbered areas are listed in Table 2, and the spectral results given in Table 3.

region was then subdivided into quadrants on north–south and east–west lines, and the extracted spectra were vignetting-corrected. We use the most recent response matrix of 1993 January, but also fitted spectra using that of 1992 March 11, the most consistent matrix before the recent recalibrations.

Raymond–Smith models (Raymond & Smith 1977, hereafter RS) were used with abundances (Anders & Grevesse 1989) equal to those used in the plasma models of Mewe, Groenenschild & van den Oord (1985) and Kaastra, hereafter MEKA (Kaastra & Mewe 1993a,b). The most important difference between the two sets of abundances is that the iron abundance is 1.48 times the value in the original solar-abundance RS models, relative to hydrogen. As our preliminary results indicate significant residuals at ~1.9 keV, we allow the silicon abundance to vary in some of our models – note that the silicon abundance differs by under 7 per cent, from $\mathrm{Si/H}=3.55\times10^{-5}$ (RS) to $\mathrm{Si/H}=3.31\times10^{-5}$ (MEKA).

The non-cluster background model follows Hasinger (1992) with three components: (i) a 10^6 K (80.8-eV) RS thermal plasma with no absorption; (ii) a 2.5×10^6 K (0.2-keV) RS thermal plasma with known flux, temperature and absorption of 5×10^{19} cm^{-2}; (iii) a power law with fixed photon index and flux $F=a\nu^{-1.12}$, where ν is frequency, and a is normalized such that the unabsorbed flux at 1 keV is 13.4 keV cm^{-2} s^{-1} sr^{-1} keV^{-1} with a column density equal to the Galactic value. Any additional absorption above Galactic required in the source model also acts on this extragalactic component. The known fluxes were scaled from the average values obtained from deep pointings by Hasinger.

All spectra from this observation also require a solar-scattered oxygen Kα line at 0.54 keV. This emission from upper-atmosphere oxygen varies strongly between observations and is highly dependent on solar activity. It can vary across the field with changing zenith angle (Snowden & Freyberg 1993). However, in background spectral fits where the line strength was free to vary, all background regions fit a line strength proportional to the area, giving a count rate of ~0.9 count s^{-1}, consistent with those found in other observations and analyses (Snowden & Freyberg 1993). We are therefore confident that the fitted line is physically plausible.

To model background emission from the cluster, one RS component was included in addition to the three existing non-cluster background components. The abundance of this extra component was fixed at 0.2 $Z_\odot$, as determined by *Ginga* (Takano et al. 1989) and the *ROSAT* All Sky Survey (Böhringer et al. 1994). The temperature was free to vary, and expected to be $kT\sim2$ keV, as found by *Ginga* (Takano et al. 1989) and *EXOSAT* (Edge 1990), and confirmed by the *ROSAT* All Sky Survey.

The final total (cluster plus non-cluster) background model we settled upon was: RS$_1$(background) + absorption (5×10^{19} cm^{-2}) $\times$ RS$_2$(background) + absorption(Galactic background) $\times$ Power–law$_3$(extragalactic background) + absorption(free) $\times$ RS$_4$(cluster background) + Gaussian$_5$(0.54-keV, solar-scattered O Kα line). This model has five free parameters: the normalizations of the three (two non-cluster and one cluster) background RS components, the RS background cluster temperature, and the normalization of the non-cluster O Kα line. When fitted to the four background spectra this model gave reduced chi-squared $\chi^2/\nu\sim1$, and consistent values of the soft background and O-line fluxes. The model parameters are given in Table 1.

Table 1. Background spectral model fluxes and temperatures. The regions are quarters of an annulus from 0°.3 to 0°.8 centred on the galaxy core. The fluxes are from 0.2 to 2 keV, include the effects of absorption on the components, and are scaled to be independent of solid angle. The flux units are 10^{-8} erg cm^{-2} s^{-1} sr^{-1}. The areas differ because of the PSPC ribs and subtraction of contaminating point sources. The pixel size is 2×2 arcmin^2. Subscripts refer to the background component list in the text. RS = Raymond–Smith thermal model, PL = power-law model. The line has an energy of 0.54 keV.

	S.E. quadrant	S.W. quadrant	N.W. quadrant	N.E. quadrant
Area (arcmin^2)	1264	1132	1104	1228
RS$_1$ flux	2.32	1.33	1.27	2.02
RS$_2$ flux	1.02	1.54	0.0621	0.588
PL$_3$ flux	3.83	3.83	3.83	3.83
RS$_4$ kT (keV)	1.76	2.09	1.89	1.76
RS$_4$ (cluster) flux	20.0	6.56	6.39	14.1
Line$_5$ flux	2.41	2.19	2.32	2.33
Total	31.34	17.54	15.76	24.63

To construct background spectra for any particular source region, we used bilinear interpolation (Press et al. 1989) between the centroids of the four quadrants and the centroid of emission of the source area to determine the spectral shape of the background within that source region. The fluxes were scaled by source region area, except the normalization of the cluster component of the background spectra which was allowed to vary to model all source (cluster and galaxy) emission. Thus in fits of the galaxy spectra we do not include a separate cluster emission component. All parameters other than the cluster RS temperature and normalization are fixed in the source models.

3.2 Source regions investigated

Table 2 defines the areas shown in Fig. 14 and gives the total flux from each region and the flux from the background components of the models used. Because of the complexity of the image, the areas were chosen visually. Region 1, to the north of the core, appears to have a lower surface brightness than areas at similar radius from the core and different position angle. Region 2, the core of M86, excludes all emission from the plume. Region 3 encompasses solely the core of the plume. Region 4 covers the inner 4 arcmin of the galaxy, centred between the plume core and the galaxy core. Region 5 is the inner 8 arcmin, and region 6 the emission in M86 out to, but not including, M84 (a radius of 15 arcmin). Region 7 covers solely M84, primarily to serve as a check on the background subtraction, and to determine if the silicon line measured in M86 is a background or fitting artefact. Region 8 has a similar size and distance from the core as region 1, but is to the south, to investigate any abundance gradient

Table 2. Source areas used in the spectral analysis; see Fig. 14. The fluxes are scaled to be independent of solid angle, units 10^{-8} erg cm^{-2} s^{-1} sr^{-1}. Note that due to the rapid decrease in surface brightness with radius, the average flux decreases for larger regions.

Region	Area arcmin^2	Total Flux	Non-cluster background Model Flux	Centroid offset (arcmin) RA	Dec.
1 N void	108	26.2	8.46	1.32	12.6
2 Core	12.9	304	8.70	0.42	0.42
3 Plume	12.7	221	8.56	0.54	3.24
4 4 arcmin	41.2	223	8.63	0.18	1.38
5 8 arcmin	223	103	8.27	−0.24	1.38
6 15 arcmin	683	59.9	8.67	0.06	0.12
7 M 84	18.8	107	8.61	−16.38	−3.66
8 S M 86/M 87	98.5	33.7	8.93	0.84	−12.24

across the field. In region 8 the surface brightness has been obviously increased by M86, but it is interesting to find out if the temperature and metal abundance are similar to either the galaxy or cluster emission.

3.3 Spectral models

As noted above, the background spectra for a particular source region were interpolated from the four quadrant spectra. These were not allowed to vary, with the exception of the cluster temperature and normalization. A fit was attempted with just these two free to change. Then, if necessary, the column density, abundance, and silicon abundance were freed (in that order) and at each stage the model was compared to the data. The silicon abundance was allowed to vary due to a distinct line-like residual observed at 1.9 keV, interpreted to be a Si XIII line (see Fig. 15). This residual is unlikely to be a particle background problem, as the observed flux returns to the model value at energies higher than the line. The linewidth is consistent with the spectral resolution of the PSPC at 1.9 keV. Three regions require a high silicon abundance, and the final model values and uncertainties given for those areas include this effect. All other parameters are from models with four free parameters – the temperature, metal abundance, normalization and column density of the single-temperature M86 emission. The fit results are shown in Table 3.

We also attempted to include a 3-keV bremsstrahlung component, as seen by *ASCA* (Awaki et al. 1994; Matsushita et al. 1994). It is only significant in region 6, but because several separate regions of differing temperature are known to be emitting in that area, it is not surprising that fitting a component at a second temperature is statistically useful. However, it remains unclear whether such a component is modelling actual bremsstrahlung emission from M86, cluster emission in front of and behind M86, or inadequacies in model spectra faced with such a complex area. A bremsstrahlung component is not significant in regions 4 or 5. *ASCA* in any case is much more sensitive to emission at this temperature, and so it is not surprising that we fail to detect

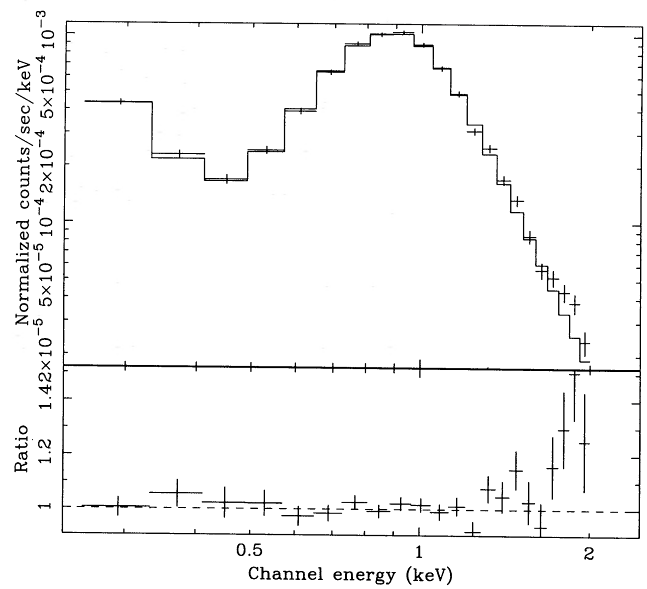

Figure 15. The significance of an emission line at 1.9 keV, which we attribute to Si XIII from sputtered dust in the ISM of M86, can be seen by the residuals in this plot. The upper panel plots the spectrum from region 4 (see Table 3), and the best-fitting model with the silicon abundance reset to the same value as all other abundances. The ratio of the residuals to the data is plotted in the lower panel and illustrates the significant residuals at 1.9 keV.

this component while *ASCA* appears to require it. Thus we do not include a bremsstrahlung component in our models.

Note that in all regions the photoabsorbing column density (N_H) fitted is consistent with the Galactic column. No regions require an extra soft emission component to allow consistency with Galactic column, nor do the normalizations of the (predominantly soft) background components appear to force the column density higher than Galactic. Each region is described below.

(i) *The northern 'void' (1)* shows no significant changes in spectral shape from interpolated cluster emission. This

Table 3. Results of the spectral analysis. All spectra use 22 bins. Model A allows fits to kT, N_H, and the metal abundance, Z, and has four free parameters (one normalization). Model B additionally allows the silicon abundance to vary and has five free parameters. Parameters are listed as value (upper limit, lower limit); limits are at 90 per cent confidence. Where model A shows $\chi^2/\nu > 1.5$ (regions 4, 5 and 6) the residuals were at around 1.9 keV and model B was used. Where model B is shown for a region, the parameter values and uncertainties listed were calculated with the silicon abundance free. Galactic column density is 2.6×10^{20} cm^{-2}. The cluster abundance is $Z \sim 0.2$ Z$_\odot$.

Region	χ^2 A	χ^2/ν A	χ^2 B	χ^2/ν B	kT keV	N_H 10^{20} cm^{-2}	Z Z$_\odot$	Si Si$_\odot$
1 N void	19.8	1.10			1.74 (2.55,1.40)	2.66 (3.33,2.08)	0.14 (0.32,0.003)	
2 Core	15.2	0.85			0.80 (0.82,0.78)	2.20 (2.61,1.72)	0.33 (0.43,0.25)	
3 Plume	15.9	0.88			0.83 (0.85,0.81)	2.10 (2.73,1.35)	0.65 (1.01,0.46)	
4 4 arcmin	29.1	1.62	19.8	1.17	0.82 (0.83,0.81)	2.03 (2.38,1.67)	0.48 (0.60,0.39)	1.07 (1.60,0.67)
5 8 arcmin	47.8	2.66	16.6	0.98	0.88 (0.89,0.87)	2.44 (2.67,2.21)	0.39 (0.44,0.35)	0.94 (1.20,0.72)
6 15 arcmin	59.7	3.32	18.3	1.08	0.94 (0.96,0.93)	2.59 (2.79,2.40)	0.30 (0.34,0.27)	0.79 (0.95,0.64)
7 M 84	25.5	1.42			0.79 (0.82,0.75)	2.90 (3.50,2.34)	0.15 (0.20,0.10)	
8 S M 86/M 87	20.2	1.12			1.13 (1.26,1.09)	3.23 (3.85,2.69)	0.17 (0.25,0.11)	

region only needs a renormalization of the interpolated cluster emission for a fit with $\chi^2/\nu \sim 1$. The normalization increases by a factor of 1.61. No change is required in N_H, kT or abundance.

(ii) *A southern region (8)* intermediate between M86 and M87 was analysed next as a background check. N_H is consistent with the Galactic column. The abundance measured in region 8 is consistent with the cluster abundance and is inconsistent with that of the core of M86 and region 3. The temperature is intermediate between the galaxy and cluster temperatures. No obvious residuals remain.

(iii) *The core (2)* shows a significantly higher abundance than the cluster abundance, with a significantly lower temperature. The temperature and overall metal abundance are typical of ellipticals of this size. If the silicon abundance is allowed to vary, then χ^2 is minimized when $Si \sim 0.73$ but the additional parameter is not statistically significant at the 90 per cent level ($1.32 < Si < 0.29$ are the 90 per cent limits). The core emission appears to be extended to the south at radii as small as 0.5 arcmin, and may therefore be affected by the ram pressure. Deprojection of *Einstein* surface brightness profiles of M86 indicates a cooling flow with a mass deposition rate of about 1 M$_\odot$ yr^{-1} (Thomas, Fabian & Nulsen 1987). We therefore attempted to detect possible cooling flow emission in M86 by fitting RS cooling flow models (Johnstone et al. 1992) to the spectrum from the core. These attempts were unsuccessful. We either saw acceptable N_H and abundance but an unacceptable fit statistic of $\chi^2/\nu \sim 5$ (from too much model emission at ~ 0.5 keV) or, if the abundance was allowed to vary, it reached the model upper limit, $Z = 2$ Z$_\odot$, inconsistent with the *ASCA* result. This behaviour is shown in Rangarajan (1995) to be characteristic of a cooling flow model fitting single temperature data. The asymmetry of the core may render it impossible to deproject under the assumption of spherical symmetry. We therefore find no evidence for a cooling flow, and the core appears to be consistent with a single-temperature model.

(iv) *The plume (3)* shows the highest metal abundance of any region and is inconsistent with both cluster and core abundances. The temperature is comparable to that of the core. Both are significantly lower than the cluster temperature.

(v) *The inner 4 arcmin (4).* To check these results from region 3 with a spectrum containing more counts, we analysed region 4. This shows an abundance intermediate between that of the core and the plume, with a similar temperature to that of both core and plume and significantly lower than the cluster temperature. A silicon line at ~ 1.9 keV is apparent, and allowing the silicon abundance to vary reduces χ^2 significantly, with 90 per cent limits of $0.67 < Si < 1.60$. *ASCA* 90 per cent limits are $0.25 < Si < 0.82$ Si$_\odot$. Thus the *ASCA* and *ROSAT* silicon abundances are compatible, and further investigation with *ASCA* should set tighter limits on spatial variation of the silicon abundance.

(vi) *The inner 8 arcmin (5).* This larger region shows a similar abundance and temperature to the core. The silicon line is again significant, similar to region 4 in both appearance and silicon abundance. Once the silicon abundance is allowed to vary, there are no significant residuals in the spectral fit.

(vii) *The inner 15 arcmin (6)* shows an abundance similar to that of the core. Although this region shows a higher temperature, it is still significantly lower than the cluster. The silicon line is also significant, similar to region 4 in appearance and silicon abundance. This region is approximately the *ASCA* SIS field of view. The *ASCA* temperature (Awaki et al. 1994) is 0.70–0.80 keV, and the metal abundance, 0.37–0.58, agrees well with the values derived here. However, we disagree on the column density: *ASCA* finds $(6–16) \times 10^{20}$ cm^{-2}, whereas these data have 90 per cent limits $(2.40 < N_H < 2.79) \times 10^{20}$ cm^{-2}. This could be due to soft emission from either M86 or M87, not accounted for in our model by a corresponding soft component because of the background complexity. Such emission will force the column densities we fit to be lower than the true value. The determination of intrinsic absorption in M86 is difficult with no obvious background region, many soft components, and high asymmetry. A cross-calibration of *ASCA* and these *ROSAT* data should reveal the absorption more clearly.

(viii) *M84 (7)* was analysed both as a check on the background model and the high silicon abundance found in M86, and as an interesting source in its own right. The temperature is similar to that of M86, and no intrinsic absorption is needed (but note the lacunae above). M84 appears to have a low metal abundance. The model is an excellent fit and does *not* show any evidence of enhanced silicon, increasing our confidence in the background subtraction and in the significance of the silicon line found in other regions.

The hole at RA offset 1.79 arcmin, Dec. offset 1.94 arcmin seen by the HRI (Section 2, Figs 5 and 6) is detected clearly in the PSPC as well. Sadly, it is difficult to obtain the spectrum of a hole, but a spectrum of the surrounding area (radius 1.5 arcmin) fits well to cluster metallicity, though consistent at 90 per cent with either cluster or galaxy core metallicity ($0.12 < Z < 0.40$). It is *inconsistent* with the plume metallicity. Both temperature and column density are consistent with the values determined for the core.

In summary, all areas are consistent with solely Galactic column density. The metal abundance increases within the galaxy and is highest in the plume where it is significantly above even the core abundance. The ISM appears to be at 0.8–0.9 keV in the core and plume, increasing to cluster temperature smoothly in the south. The northern 'void' appears to be cluster emission with a slightly higher flux than expected from the interpolation. An enhanced silicon abundance is detected at around solar abundance in all large-scale fits of M86 spectra, but is not detected in M84.

Following the advice from the referee, we advise caution in the overinterpretation of abundance variations. The spectral resolution of the PSPC cannot discriminate between emission from a multiphase gas and emission from an isothermal gas, which could lead to erroneous abundance determinations. For example, fake PHA data from two different RS emission components can be constructed (by fitting region 2 with the standard single RS and background model with an additional RS component – the temperature was arbitrarily set to that of the cluster at 2.4 keV, and the abundances of both components were set to the solar value). A good fit can then be obtained by fitting the fake data with the standard background model, and the single RS component with free abundance. The best fit gave a temperature that was similar to the lower temperature used in the multiphase model, but the abundance determination was $Z = 0.45$ – significantly lower than the solar values used in each of the dual-phase components used to create the fake data. To resolve such a problem in abundance determinations, data from *ASCA* will be required to discriminate multiphase contributions to the emission. Not only does the spectral resolution of *ASCA* enable resolution of individual emission lines but its band-pass extends up to 10 keV, covering the break in the bremsstrahlung emission from the hotter cluster component. Despite these problems with abundance determinations, we emphasize that our following discussion is not invalidated by these effects, especially that pertaining to the enhanced silicon abundance which was resolved as an individual line in the PSPC data (see Fig. 15).

4 DISCUSSION

Both the PSPC and HRI observations show the same structures, which are very similar to those present in the *Einstein* image, but at much higher signal-to-noise ratio. We are particularly interested in the origin of gas in different emission regions, in possible pressure differences between regions, and in placing limits on the velocity of M86 in the plane of the sky. Fig. 16 shows the PSPC contours superimposed on an optical image of M86. The plume and the optical asymmetry towards the north-west have similar directions and extents. The X-ray core has the same position as the optical core (White et al. 1991) to within 13 arcsec.

We can calculate a lower limit on the pressure difference between the high surface brightness plume and the northern 'void' across the sharp edge. The surface brightness differs by a factor of 10 within 4 arcmin. The temperature and abundance of the two areas differ (Table 3), and evaluating RS models with these parameters gives a cooling rate Λ, where $\Lambda_{\rm plume} \sim 1.8\Lambda_{\rm void}$. As the surface brightness we detect is given by $\Lambda n^2 d$, where d is the depth of the emitting gas along the line of sight, the most conservative assumption that the depths of the void and plume are equal ($d_{\rm void} = d_{\rm plume}$), implies that the density of the void is a factor of 2.4 lower. Thus the pressure in the plume $nT_{\rm plume} \sim 1.1 nT_{\rm void}$, using the temperatures derived spectrally above. Given these simplistic assumptions, these results are consistent with pressure balance between the two regions. If we assume that only flux in *excess* of the interpolated cluster value is emitted in a depth $\sim d_{\rm plume}$, we ascribe only 40 per cent of the observed void emission to that volume (the normalization in the void is

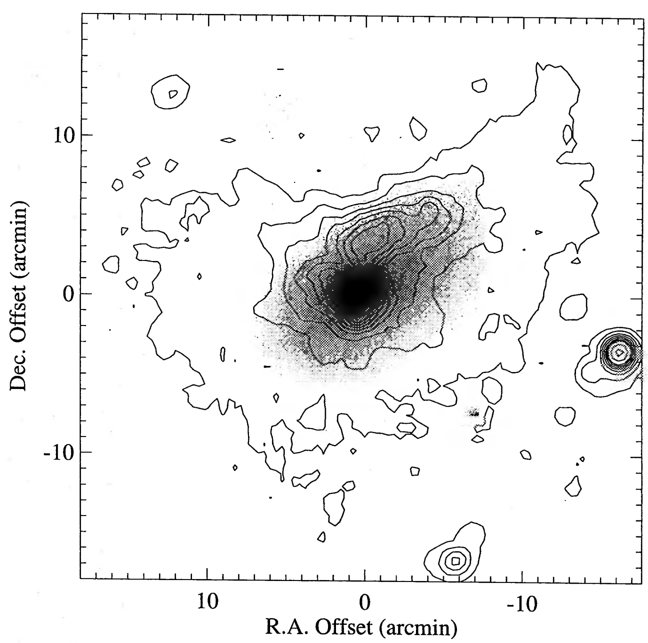

Figure 16. An optical *J*-band image of M86, under a contour map of top-hat fixed-scale smoothed PSPC data. The optical centre derived by isophote fitting is RA $12^{\rm h}26^{\rm m}12^{\rm s}$, Dec. $12°56'47''$ (White et al. 1991), 13 arcsec south of the X-ray pointing. The optical image is smaller: it is only plotted within ± 7.5 arcmin of the centre. A small galaxy can be seen in the optical image 2 arcmin to the north-east of M86.

a factor of 1.61 larger than the interpolated cluster value). This implies a factor of 25 change in surface brightness and that $nT_{\rm plume} \sim 1.8nT_{\rm void}$. However, the depth of the void could be much larger than the depth of the plume. It is therefore possible that the pressure in the void could be lower, and that a larger pressure difference exists. We therefore conclude that these data are consistent with pressure equilibrium between the plume and the void, but the void may be at a lower pressure if projection effects are important.

We considered several possible origins for the gas and the observed surface brightness in the northern 'void'.

(1) *The M86 ISM heated to cluster temperature*. However, the metal abundance in the void is inconsistent with the core or plume abundance and consistent with the cluster abundance. If gas in the void was heated galactic gas, it seems unlikely that the northern edge wuld be as abrupt as it is, unless it is a shock front which is not observed in the X-ray or in any other waveband, and in the opposite direction to the possible direction of motion of the galaxy in the plane of the sky. This therefore seems unlikely.

(2) *ISM emission with high absorption* $N_{\rm H} \sim 10^{23}$ cm^{-2}. The foreground cluster emission would be absorbed by only our local column density of 2.6×10^{20} cm^{-2}. The high $N_{\rm H}$ only allows photons above 2 keV to pass, i.e. above the *ROSAT* band. However, a column density of 10^{23} cm^{-2} above the void, over an area of 108 arcmin$^2 \sim 3900$ kpc^2, means that the mass of cold gas required is at least 1.7×10^{12} M$_\odot$, which is larger than the mass of the whole galaxy. Even allowing an obscured region with a tenth of the area, close to the edge, would still imply a mass of cold gas larger than the mass of the visible ISM. Thus we do not believe that absorption can cause the 'void'.

(3) *Plume material, obscured by a high column*. If we fix the source flux in the void to equal that in the plume, there is no column density that allows an even remotely acceptable fit. If we then allow the flux to vary, it fits with ~ 60 per cent of the interpolated cluster flux, but with clear residuals at 0.5 keV. If we then allow the temperature and abundance to vary, the best parameters are similar to the cluster abundance and temperature. These spectra do not allow any plume material in the void.

(4) *Cluster emission filling in the void left by the passage of M86*. In this region, the cluster flux is only 1.61 times the interpolated cluster emission value. M86 may have some southwards velocity as well as radial. If it leaves an evacuated Mach cone behind that is filled with cluster gas rushing in, turbulence may lead to slightly enhanced emission but otherwise little change. We discuss this possibility in greater depth later.

We can derive a lower limit to the mass of plume, assuming that it has a similar thickness to its width. The luminosity of the plume is $L_{\rm plume} \sim 2\times10^{41}$ erg s^{-1} (assuming a distance of 20 Mpc). Using the abundance and temperature measured in region 3 to find the emissivity, the plume density is 4×10^{-3} cm^{-3}, and the plume mass is $M_{\rm plume} \approx 2\times10^9$ M$_\odot$, assuming a plume width and depth of 25 kpc and length 50 kpc. The mass of the ISM in the core of M86, similarly derived, is $M_{\rm core} \approx 8\times10^8$ M$_\odot$ for a core luminosity of 1.5×10^{41} erg s^{-1} within a radius of 2 arcmin ~ 12 kpc. The core density (assuming homogeneity, thus an upper limit) is 9×10^{-3} cm^{-3}. It appears from this that the plume has at least twice the mass of the core, and therefore the hypothesis that the ISM is being removed from M86 in a single blob is supported (Takeda et al. 1989), allowing the disruption time-scales by ram pressure and the hot ISM to be long. The mass of dust required to pollute the plume from the core abundance to the observed value is $\sim 10^6$ M$_\odot$, assuming solar abundance to have a metal number density $\sim 10^{-4}$ compared to hydrogen. This mass is consistent with the observed H I mass in the plume of 2.5×10^8 M$_\odot$ (Bregman & Roberts 1990) assuming a gas-to-dust ratio of $M_{\rm gas}/M_{\rm dust} \sim 150$. White et al. (1991) estimate the mass of dust directly from the *IRAS* fluxes to be 10^4–10^5 M$_\odot$, but they note that it is severely affected by small-grain temperature fluctuations and uncertainties in grain opacities (Draine 1989).

Assuming an average density of 10^{-3} cm^{-3} in the whole of region 6, an upper limit on the mass of the ISM assuming spherical symmetry is $\sim 4\times10^{10}$ M$_\odot$. The mass of silicon in the region if at solar abundance is 2×10^7 M$_\odot$, assuming a Si-to-H number ratio of 3.5×10^{-5}. This is consistent with the stellar mass loss expected $\dot{M}$(stellar) ~ 1 M$_\odot$ yr^{-1}, operating over the orbital period of M86, 10^9 yr (Forman et al. 1979), and a gas-to-dust ratio of $M_{\rm gas}/M_{\rm dust} \sim 150$.

The cooling time-scale of gas, assuming bremsstrahlung and line radiation from the plasma (Fabian et al. 1980), is

$$t_{\rm cool} \sim 4\times10^6 (T/10^7\,{\rm K})^{3/2}\,(n\,{\rm cm}^{-3})^{-1}\,{\rm yr},$$

using the RS approximation to the cooling curve,

$$\Lambda = 10^{-19}T^{-1/2} + 2\times10^{-27}T^{1/2}\,{\rm erg\,cm^{-3}\,s^{-1}};$$

this gives $t_{\rm cool,plume} \approx 9\times10^8$ yr, $t_{\rm cool,core} \approx 4\times10^8$ yr. The disruption time-scale of the plume by the ram-pressure is $t_{\rm dis} \sim 5\times10^8$ yr (using the equations in Takeda et al. 1984), assuming that a large fraction of the ISM is carried off almost intact. This disruption time-scale is linearly dependent on the radius of the plume. If the plume is fragmented into smaller pieces when stripped, the disruption time-scale may be much lower than the time for it to move the observed displacement. Thus both observation and these considerations indicate that the ISM of M86 is being stripped in a single blob.

One interesting question these data can address is that of the velocity of M86 in the plane of the sky. The sound speed in cluster gas is $c_{\rm s} \approx 10^4\,(T\,{\rm K})^{1/2}$ cm s^{-1}; at the observed cluster temperature of $kT \approx 2$ keV, $c_{\rm s} \approx 500$ km s^{-1}. The radial velocity of M86 is -1374 km s^{-1}, implying that the interaction of the ISM of M86 with the cluster gas is supersonic. One explanation for the morphology, temperatures and abundances observed in M86 is that we may be seeing the Mach cone to the north of the galaxy, and therefore that the galaxy has a significant velocity in the plane of the sky. The morphology (Fig. 2) shows enhanced emission both to the east and west of the core (the plume and the north-east arm). The low surface brightness northern void appears to be symmetrical about north–south. We therefore assume that the most likely direction for the velocity of M86 is to the south. The opening half-angle of a Mach cone is ϕ where $\tan(\phi) = c_{\rm s}/v_{\rm gal}$, where $v_{\rm gal}$ is the velocity of the galaxy. The opening half-angle projected on the sky ϕ' is similarly $\tan(\phi') = c_{\rm s}/v_{{\rm gal}\perp}$ where $v_{{\rm gal}\perp}$ is the velocity perpendicular to our line of sight.

Fig. 2 shows an opening angle $\sim 90°$ from centre of galaxy along the north-eastern arm and to the south of the plume, implying $v_{{\rm gal}\perp} \sim c_{\rm s}$. It appears that the apex of the cone is obscured by the plume. Another indication of the minimum

$v_{\mathrm{gal}\perp}$ is the separation of the plume from the core. If $v_{\mathrm{gal}\perp}$ is much less than $v_{\mathrm{gal}\parallel}$, we will not see any separation of plume on the sky, assuming that the plume is extended back along the path of the galaxy (Takeda et al. 1984). The plume separation, and the cluster abundance and low surface brightness of the northern void argue that $v_{\mathrm{gal}\perp} > 500$ km s^{-1} and may be comparable with $v_{\mathrm{gal}\parallel}$. An upper limit on $v_{\mathrm{gal}\perp}$ is given by the minimum cone angle $\phi' > 70°$ giving $v_{\mathrm{gal}\perp} > 700$ km s^{-1}. Therefore the total velocity of M86 may be $1460 < v_{\mathrm{gal}} < 1540$ km s^{-1}. This is over twice the cluster velocity dispersion, implying that M86 may not be bound to the core of the Virgo cluster, or that the cluster mass-to-light ratio increases at large radii from M87.

This scenario can explain the morphology. The high pressure to the south of M86 is forcing the ISM south of the core to be denser and increases the emissivity. The southern extension has a surface brightness a factor of 2 brighter than the east or west at similar radii. Thus an increase in the pressure of gas to the south of the core, increasing the density by ~ 40 per cent, is sufficient to explain the morphology of the core. The flux from the extension is about 5 per cent of the flux from the plume; given the plume mass of $\sim 2\times 10^9$ M$_\odot$, we expect the extension to have a mass of $\sim 10^8$ M$_\odot$. The pressure of the ISM in the core of M86 is $nT \sim 10^5$ K cm^{-3} using a core density of 0.01 cm^{-3} (Thomas et al. 1987) and a temperature 0.8 keV. The ram pressure of the galaxy moving at a total velocity of ~ 1500 km s^{-1} through the ICM (density $\sim 10^{-4}$ cm^{-3}; Stewart et al. 1984) is $P_{\mathrm{ram}} \sim 3\times 10^4$ K cm^{-3}, a factor of 3 less than the ISM pressure and thus not enough to disturb the core itself. The mass swept up by the core of the galaxy (inner 1 arcmin) moving through the core of the cluster [core radius = 600 kpc (Forman et al. 1979), density 10^{-4} cm^{-3}] is $\sim 10^8$ M$_\odot$, which is comparable to the mass expected within the southern extension. Thus the increase in pressure to the south and an increased density resulting from the 'snow plough' effect of M86 on the cluster gas may be responsible for the emission to the south of the core.

In this scenario the low surface brightness to the north of the core is due to the projection of the Mach cone drawn by M86 as it dives into the cluster. The evacuation and refilling by cluster gas of the Mach cone is consistent with the spectra from the northern void, the low surface brightness, and the morphology of the area. As the cone is seen with M86 projected close to the edge, this implies that the inclination of the direction of movement of M86 to our line of sight is similar to the real opening half-angle of the cone. The plume is produced only when M86 enters the core of the cluster, whereas the Mach cone is produced during interaction with the outer part of the cluster and thereafter. Thus the plume may be a relatively late addition to the morphology we observe, as M86 hits the core of the cluster. The reason that we observe less ejecta from the galaxy to the north is that to the east and west we are looking along the edge of the cone with high column density of ejecta; to the north the column is low because of the cone inclination. The ejecta will move up the major axis of the galaxy seen in the optical image (Fig. 16), as this is the most gradual way out of the galaxy potential. This effect may produce the displacement of the plume towards the west, and may be augmented by the higher cluster pressure to the south-east, nearer the cluster core. The hole may be produced when a tongue of the low-abundance, high-temperature cluster gas which is removing the plume intrudes between the core and the plume as the plume completely detaches. This cluster material has a much lower emissivity, similar to that of gas in the northern void, and may thus produce a low flux while maintaining pressure balance. Another possibility is that the small galaxy seen in Fig. 16 2 arcmin to the north-east of M86 may have a high photoelectric column density and absorb the emission from M86. The optical position of the small galaxy lies 2 arcmin southwest of the hole centre, but it may also be being stripped and thus the ISM position may not be coincident with its optical position.

The inferred inclination of the Mach cone is consistent with the velocity $v_{\mathrm{gal}\perp}$ inferred from the projected opening angle $v_{\mathrm{gal}\perp} \sim 500$ km s^{-1}, giving a Mach cone opening half-angle of 18° using the total velocity. The ratio of $v_{\mathrm{gal}\perp}$ to $v_{\mathrm{gal}\parallel}$ will produce an inclination of the path of M86 to our line of sight of $\sim 18°$, which would place M86 over one edge of the cone, as observed. Thus the velocity inferred from the cone opening angle agrees with the observed position of the galaxy relative to the cone.

We anticipate a high velocity from theoretical ram-pressure stripping arguments. The velocity dispersion of M86 is 256 km s^{-1} (Roberts et al. 1991). Stripping of the whole galaxy occurs when $\rho_{\mathrm{clus}} v^2 > \rho_{\mathrm{gal}} \sigma^2$ (Gunn & Gott 1972; Forman et al. 1979), and $\rho_{\mathrm{clus}} \sim 10^{-4}$ cm^{-3}, $\rho_{\mathrm{gal}} \sim 0.01$ cm^{-3}; therefore if we see complete stripping, it is likely that the total velocity of M86, v_{gal}, is greater than $10\sigma \sim 2500$ km s^{-1} (σ is the velocity dispersion). This and the arguments above for a non-zero $v_{\mathrm{gal}\perp}$ indicate that the total velocity of M86 may be up to a factor of 2 higher than the radial velocity, and therefore that M86 may not be bound to the Virgo cluster. However, it does not appear that the very core of M86 is being stripped out; thus 2500 km s^{-1} is a hard upper limit.

White et al. (1991) find that the *IRAS* fluxes and flux ratios at the displaced source are consistent with their hypothesis of dust sputtering in the displaced plume gas, raising the dust to a higher temperature. The significantly increased abundance in the plume over both core and cluster abundances and the similar temperature to the core support this scenario. If dust is being destroyed because of disruption of the cold gas clouds which previously contained it, the embedded metals will be released to the ISM, which will raise the observed abundance. The *IRAS* sources are of order 2 arcmin across, and the 60-μm emission is coincident with the plume. The unexpected detection of a silicon line, implying a high silicon abundance in all the large-scale spectra, suggests that the process of dust destruction and emission by the resulting metals may have been occurring for a time similar to that for the ram-pressure stripping. The large area of high silicon abundance also points to the possibility that this process may be happening at larger radii than just near the *IRAS* detection. The mass of silicon in this area is consistent with mass of dust in the galaxy. The high plume abundance, supporting the presence of dust in the plume therefore also supports the hypothesis that the north-west extension in the optical isophotes of M86 is due to scattering of starlight from a high dust concentration. Because M86 is one of the few early-type galaxies where dust and cold gas may be detectable due to the disruption, other early-type galaxies may contain similar large amounts of dust and cold gas, hidden from observation (Rangarajan & Fabian

1995). Such absorption deep in an elliptical galaxy has been detected in NGC 1399 (Rangarajan et al. 1995), with a cold gas column density $N_{\rm H} \sim 10^{21}$ cm^{-2}. Early-type galaxies may contain much more cold gas and dust than previously thought.

Alternative scenarios for the morphology of M86 have been suggested. Bregman & Roberts (1990) argue that the velocity difference between plume H I and core H I is too low to allow ram-pressure stripping. However, White et al. (1991) have shown that if the stripped gas is a large fraction of the ISM of the galaxy and does not fragment, then the acceleration expected from the ram pressure and the distance travelled both agree well with the velocity difference and the physical separation observed. Bregman & Roberts suggest that conductive evaporation of an H I plume, lowering the temperature and so increasing the emissivity of a part of the ISM in a cooling flow, may explain the plume. However, we observe directly the temperature to be similar in both plume and core. The higher abundance in the plume (0.65 as compared to 0.33 in the core) increases the emissivity by at most a factor 1.5. Therefore this cannot explain the increase in surface brightness of the plume by a factor of up to 5 over that expected for an undisturbed galaxy ISM (Fig. 10) and shows that there must be an increase in the density. The possibility of a tidal interaction with NGC 4402 (if it is in fact close and not merely projected near to M86 on the sky) also seems unlikely given the complex morphology that we observe, the high velocity of M86 relative to the cluster, and the cooling and dissipation time-scales of the plume material. If tidal disruption was the cause of the ISM structure, we would expect a similar effect on the stellar component of M86, whereas no correlation is observed between the structure here and the stellar distribution. Ram-pressure stripping appears to be the only viable mechanism for producing the plume in M86, and it explains the observed morphology. Dust destruction within the stripped material accounts for both the *IRAS* 60-μm source observed displaced from the core of the galaxy, the optical asymmetry, and the enhanced abundance we observe in the plume.

5 SUMMARY

From a spectral analysis of *ROSAT* PSPC data on M86 we detect a high metal abundance in the X-ray plume, $Z \sim 0.65^{+0.4}_{-0.2}$ Z$_{\odot}$. This is significantly higher than the abundance in the core of M86, or the cluster abundance. The galaxy and the plume are at similar temperatures $kT \sim 0.8 \pm 0.03$ keV, compared to the cluster temperature of ~ 1.9 keV detected in all surrounding areas and consistent with the other observations of the cluster. The abundances and temperatures derived from the large-area spectra are consistent with *ASCA* and other previous measurements, but we map these in greater spatial detail. Spectra of the whole galaxy and surrounding regions show a significantly enhanced silicon abundance, which is not detected in the surrounding cluster emission nor in M84. The high abundance in the plume and the silicon line detected are consistent with dust destruction in the stripped gas, as cold gas in the plume is disrupted and the dust within sputtered by the hot ISM. Using both HRI and PSPC observations, we detect four structures in the X-ray emission around the galaxy: a region of low surface brightness to the north, an arm of increased emission to the north-east, a brightening of the core to the south, and the X-ray plume. These structures and the abundance measurements support the hypothesis of ram-pressure stripping of the ISM of M86 by the Virgo ICM, in a single blob. The morphology and calculations of the ram pressure indicate that M86 may have a southwards velocity in the plane of the sky of ~ 500 km s^{-1} compared to its radial velocity of 1374 km s^{-1} relative to the cluster. This result indicates that other early-type galaxies may contain larger amounts of cold gas and dust than previously thought.

ACKNOWLEDGMENTS

We particularly thank Roderick Johnstone for discussion about statistical significances, and Stefan Döbereiner for use of the PSPC data. We also thank Steven Allen and Hans Böhringer for useful criticism and much discussion, and the referee, Claude Canizares, for useful comments, especially regarding abundance determinations. ACF thanks the Royal Society for support. This research has made use of the UK *ROSAT* Data Archive Centre at the Department of Physics and Astronomy, Leicester University. We used the XSPEC and ASTERIX software packages, and thank their creators and maintainers.

REFERENCES

Abramowitz M., Stegun I. A., 1965, Handbook of Mathematical Functions. Dover, New York

Anders E., Grevesse N., 1989, Geochimica et Cosmochimica Acta, 53, 197

Awaki H. et al., 1994, PASJ, 46, L65

Böhringer H., Briel U. G., Schwarz R. A., Voges W., Hartner G., Trümper J., 1994, Nat, 368, 828

Bregman J. N., Roberts S., 1990, ApJ, 362, 468

Bregman J. N., Roberts S., Giovanelli R., 1988, ApJ, 330, L93

Draine B. T., 1989, in Thronson H. A., Shull J. M., eds, The Interstellar Medium in Galaxies, p. 483

Edge A. C., 1990, PhD Thesis, Univ. Leicester

Fabbiano G., Gioia I. M., Trinchieri G., 1989, ApJ, 347, 127

Faber S. M., Wegner G., Burstein D., Davies R. L., Dressler A., Lynden-Bell D., Terlevich R. J., 1989, ApJS, 69, 763

Fabian A. C., Schwarz J., Forman W., 1980, MNRAS, 192, 135

Forman W. R., Schwarz J., Jones C., Liller W., Fabian A. C., 1979, ApJ, 234, L27

Gunn, J. E., Gott J. R., 1972, ApJ, 176, 1

Hasinger G., 1992, in Barcons X., Fabian A. C., eds, The X-ray Background, Cambridge Univ. Press, Cambridge, pp. 229–239

Johnstone R. M., Fabian A. C., Edge A. C., Thomas P. A., 1992, MNRAS, 255, 431

Kaastra J. S., Mewe R., 1993a, Legacy - HEASARC, May 1993, No. 3, p. 16

Kaastra J. S., Mewe R., 1993b, A&AS, 97, 443

Knapp G. R., Guhathakurta P., Kim D. W., Jura M., 1989, ApJS, 70, 329

Matsushita K. et al., 1994, ApJ, 436m, L41

Mewe R., Groenenschild E. H. B. M., van den Oord G. H. J., 1985, A&AS, 62, 197

Nulsen P. E. J., Carter D., 1987, MNRAS, 225, 939

Press W. H., Flannery B. P., Teukolsky S. A., Vetterling W. T., 1989, Numerical Recipes, Cambridge Univ. Press, Cambridge

Rangarajan F. V. N., 1995, MNRAS, submitted

Rangarajan F. V. N., Fabian A. C., 1995, MNRAS, submitted

Rangarajan F. V. N., Fabian A. C., Forman W. R., Jones C., 1995, MNRAS, 272, 665

Raymond J. C., Smith B. W., 1977, ApJS, 35, 419 (RS)
Roberts M. S., Hogg D. E., Bregman J. N., Forman W. R., Jones C., 1991, ApJS, 75, 751
Snowden S. L., Freyberg M. J., 1993, ApJ, 404, 403
Stark A. A., Gammie C. F., Wilson R. W., Bally J., Linke R. A., Heiles C., Hurwitz M., 1992, ApJS, 79, 77
Stewart G. C., Canizares C. R., Fabian A. C., Nulsen P. E. J., 1984, ApJ, 278, 536
Takano S. et al., 1989, Nat, 340, 289
Takeda H., Nulsen P. E. J., Fabian A. C., 1984, MNRAS, 238, 523
Thomas P. A., Fabian A. C., Nulsen P. E. J., 1987, MNRAS, 228, 973
White D. A., Fabian A. C., Forman W., Jones C., Stern C., 1991, ApJ, 375, 35
White D. A., Fabian A. C., Allen S. W., Edge A. C., Crawford C. S., Johnstone R. M., Stewart G. C., Voges W., 1994, MNRAS, 269, 589